Improved Modulation for Three-Phase Series-End Winding Voltage-Source Inverters

Journal:	*Transactions on Industrial Electronics*
Manuscript ID	24-TIE-1777
Manuscript Type:	Regular paper
Manuscript Subject:	Machines and Drives
Keywords:	open-end winding machine, series-end winding, dead-time compensation
Are any of authors IEEE Member?:	Yes
Are any of authors IES Member?:	Yes

Improved Modulation for Three-Phase Series-End Winding Voltage-Source Inverters

Zhi Chen, You Zhou, *Member*, Feifan Guo, and Christopher H. T. Lee, *Senior Member*

***Abstract*—To extend the speed range and reduce power electronics devices of the open-end winding permanent magnet synchronous machine (OEW-PMSM) drive system, series-end winding topology is adopted in this paper. A simplified modulation strategy is proposed. Compared with space vector pulse width modulation (SVPWM), the proposed modulation calculates the four bridges' duty cycles in the ABC reference frame. It avoids complex sector identification and voltage vector distribution calculation, and controller design can be simplified. The asymmetry of the series-end winding topology results in asymmetric three-phase dead-time voltage errors. The characteristics of dead-time is analyzed, and a novel dead-time compensation strategy is proposed to eliminate current harmonics. The adaline neural network (ANN) algorithm is applied for harmonic extraction and serves as phase shifting generator, and closed-loop control of one-dimensional zero-sequence harmonics can be conducted in rotating reference frames. Simulations and experimental results verify the effectiveness of the proposed modulation and dead-time compensation method.**

***Index Terms*—Open-end winding machine, series-end winding, voltage modulation, dead-time compensation.**

I. Introduction

DUE to its expanded operating range and enhanced fault tolerance, open-end winding permanent magnet synchronous machines (OEW-PMSM) have received widespread research and application [1]–[3].

The dual-three-phase inverter is a typical driver topology for OEW-PMSMs as shown in Fig. 1a. This inverter configuration utilizes 6 bridges, comprising 12 switching devices, with each pair of bridges driving one phase of the machine. Compared with conventional star-connected winding drivers, the dual-three-phase inverter doubles the DC voltage utilization. The achievable voltage vectors are denoted by the blue dots in Fig. 2. The dual-three-phase topology offers the maximum control flexibility with $2^6 = 64$ switching states. The voltage vectors generated by the dual-three-phase inverter can be considered as the superposition of vectors generated by two standard three-phase inverters, and voltage modulation can be conducted in a two-dimensional space, namely the $\alpha\beta$ reference frame. To suppress zero-sequence currents, an angle-shifted-based distribution method is proposed in [4]. The reference voltage is divided into two vectors with the same amplitude and 120° electrical angle shift. The middle hexagon space vector modulation applied in [5] has the same performance. Furthermore, to minimize switching losses, an alternate subhexagonal center pulse width modulation is applied in [6], maintaining fixed switching states for one three-phase inverter within each control cycle.

To reduce the usage of switching devices, dual-three-phase inverter can be replaced by series-end winding driver [7]–[9]. The voltage vectors generated by this alternative configuration are depicted by the red dots in Fig. 2. Compared with dual-three-phase inverter, series-end winding driver maintains the same utilization of DC voltage in $u_0 = 0$ space. It means that the extension of operating range and the reduction of power electronics devices can be achieved simultaneously. However, this configuration compromises control flexibility by omitting two bridges, limiting its ability to produce some voltage vectors achievable by dual-three-phase inverters. As shown in Fig. 2, the only two vectors directed along the zero-axis, namely $(u_\alpha, u_\beta, u_0) = (0, 0, u_{dc})$ and $(0, 0, -u_{dc})$, cannot be generated by the series-end winding driver. It means that zero-sequence voltage cannot be adjusted by distributing zero voltage vectors within one control cycle. Furthermore, the maximum zero-sequence voltage generated by the dual-three-phase inverter is u_{dc}, while the series-end winding driver's zero-sequence voltage modulation ability is limited. The maximum voltage produced by the inverter is $\frac{1}{3}u_{dc}$. Overall, the series-end winding driver is suitable for applications where the need for zero-sequence modulation is modest but wide operating range and low cost are prioritized.

OEW-PMSMs provide a path for zero-sequence currents, and zero-sequence closed-loop control should be taken into consideration. Because the series-end winding drivers cannot

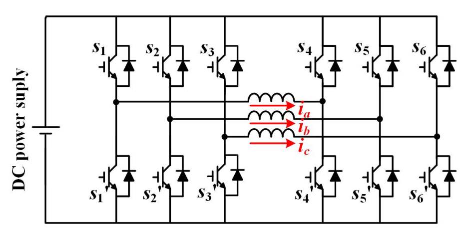

(a) Dual-three-phase driver.

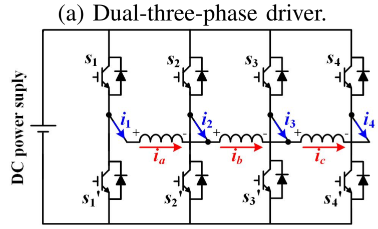

(b) Series-end winding driver.

Fig. 1: Inverter topology.

generate voltage vectors along the zero-axis, the synthesis of voltage vectors should be conducted in three-dimensional space. A model predictive current control method for OEW-PMSM is designed according to the current control cost function in three-dimensional space in [10]. Additionally, a three-dimensional space vector modulation strategy is proposed in [11]. The modulation can be conducted in ABC and $\alpha\beta0$ reference frames, and three voltage vectors for reference voltage vector synthesis can be selected. The implementation of the three-dimensional space vector pulse width modulation (SVPWM) include three steps [12]:

1) All possible switching states of the inverter and corresponding voltage vectors should be listed as shown in Fig. 2.
2) Find the basis voltage vectors that can be used to synthesize the reference voltage vector.
3) Calculate the duty cycle of each vector according to the projection of the reference voltage vector onto the basis vectors.

Without voltage vectors in the zero-axis direction, the three-dimensional space should be divided into multiple irregular tetrahedrons. It leads to challenging selection of basis vectors and complicates controller design.

This paper focuses on the series-end winding inverter and proposes an simplified modulation strategy. The paper is arranged as follows: The proposed modulation strategy for series-end winding inverter is presented in Section II. Then, the asymmetry of the dead-time effect is analyzed in Section III, and a compensation method for the asymmetric dead-time voltage error is proposed. Experimental setup and results in Section IV verify the effectiveness of the proposed modulation and dead-time compensation method.

II. Modulation Strategy for Series-End Winding Inverter

A. Proposed Modulation Strategy.

The topology of the series-end winding inverter is depicted in Fig. 1b. In this configuration, the second and third bridges are shared by phase AB and BC, while the first and fourth bridges exclusively serve phase A and C. Because current sensors are installed on the inverter's bridges, the measurements reflect bridges' outputs rather than three-phase currents. Phase currents can be calculated as follows:

$$\begin{cases} i_a = i_1 \\ i_b = i_1 + i_2 \\ i_c = -i_4 \end{cases} \tag{1}$$

The neutral point of a three-phase star-connected PMSM is in a floating state, and the voltage of each phase is determined by the switching states of all bridges. In contrast, the phase voltages of a series-end winding OEW-PMSM can be directly calculated according to the duty cycles of the bridges on both sides. Three-phase voltages can be expressed as:

$$\begin{cases} u_a = (s_1 - s_2) \cdot u_{dc} \\ u_b = (s_2 - s_3) \cdot u_{dc} \\ u_c = (s_3 - s_4) \cdot u_{dc} \end{cases} \tag{2}$$

where s_1, s_2, s_3, s_4 represent the duty cycles of the upper switches on four bridges respectively. It is evident that the three-phase voltages can be directly adjusted by modifying s_1, s_2, s_3 and s_4. What's more, because the three phases are decoupled, modulating the three-phase voltages in ABC reference frame has the same effect as modulating α-, β- and 0-axis voltages in the three-dimensional space.

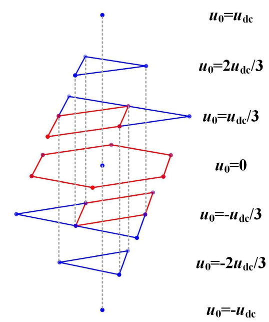

Fig. 2: Voltage vectors generated by different inverters.

According to three-phase reference voltages, the differences in duty cycles between the bridges can be calculated. By assigning an initial value to the duty cycle of the first bridge s_1, the subsequent duty cycles s_2, s_3, and s_4 are derived. The MATLAB code for calculating the duty cycles is as follows:

```
s1 = 1;
s2 = s1-ua/udc;
s3 = s2-ub/udc;
s4 = s3-uc/udc;
```

The inverter's driving signals are generated by comparing the triangular carrier signals with the reference values. To reduce switching losses, the maximum reference value among the four bridges can be set as TBPRD (timer's period in DSP):

```
smax = max([s1, s2, s3, s4]);
cmp1 = (s1-smax+1)*TBPRD;
cmp2 = (s2-smax+1)*TBPRD;
cmp3 = (s3-smax+1)*TBPRD;
cmp4 = (s4-smax+1)*TBPRD;
```

The driving signals for the four upper switches are shown in Fig. 3a. s_2 remains high throughout one control cycle, indicating that the switching state of the second bridge remains unchanged. When the minimum reference value is set as 0, the driving signal s_3 remains low as shown in Fig. 3b. Regardless of the reference voltage, setting the maximum reference value as TBPRD or minimum value as 0 ensures that at least one bridge's switching state remains unchanged within one control cycle. On the other hand, the zero voltage vectors can be evenly distributed on both ends and in the middle of a control cycle, with corresponding driving signals shown in Fig. 3c. When the three-phase voltages of the OEW-PMSM are symmetrical and sinusoidal, it can be deduced that $u_a + u_b = u_c = 0$. It means that the driving signals of the first bridge and the fourth bridge are identical. The duty cycle differences between the first and second, second and third, third and fourth bridges correspond to the three-phase voltages.

In the subsequent sections, the modulation strategy of maintaining the upper switch turned on as the fixed switching state is referred to as "Modulation I", that of maintaining the upper switch turned off is referred to as "Modulation II", and that without fixed switching states is referred to as "Modulation III".

Modulation III, which evenly distributes zero-voltage vectors, and modulation I and II, which maintain fixed switching states, differ not only in switching losses but also in other two aspects:

1) Due to the concentrated distributing way of zero voltage vector, modulation I and II will lead to more high-frequency current harmonics.
2) Different modulations lead to different voltage errors caused by dead-time.

III. Dead-time Compensation

A. Dead-time Voltage Error.

Dead-time is vital to prevent short-circuiting across inverter bridges. The adopted method in this paper is to delay the driving signals' rising edge for a dead-time interval T_d. The voltage error of a bridge caused by the dead-time is correlated with the bridge's output current rather than phase currents. Dead-time voltage error can be expressed as follows [13]:

$$e_x = -\frac{T_d}{T_s} \cdot u_{dc} \cdot \operatorname{sgn}(i_x) \tag{3}$$

where x represents the index of the bridge. The calculated voltage error is the output error of a single bridge, and the three-phase voltage errors can be expressed as:

$$\begin{cases} e_a = e_1 - e_2 \\ e_b = e_2 - e_3 \\ e_c = e_3 - e_4 \end{cases} \tag{4}$$

The second and third bridges are shared by phase AB and BC, while the first and fourth bridges are individually used by phase A and C. It leads to asymmetrical three-phase dead-time voltage errors. Taking modulation III as an example, when the d-axis current is given as 0, three-phase currents and voltage errors e_a, e_b, e_c are shown in Fig. 4a. The harmonic analysis of voltage errors is illustrated in Fig. 4b. The voltage errors of the first and forth bridge depend on the current directions in phase A and C, while the voltage errors of the second and third bridge are determined by the current relationships between phase AB and phase BC. The voltage error of phase A and C are consistent, while the voltage error of phase B differs from those in phases A and C.

When modulation I or II is adopted, at least one bridge's switching state remains fixed within one control cycle. During this period, the output voltage of the bridge will not be affected by dead-time effect. The dead-time voltage with modulation I and II can be considered as injecting additional harmonics into that of modulation III. When i_d reference is given as 0, the output currents of the four bridges can be expressed as:

$$\begin{cases} i_1 = i_q \cos(\theta) \\ i_2 = -\sqrt{3} i_q \cos(\theta + \frac{\pi}{6}) \\ i_3 = -\sqrt{3} i_q \sin(\theta) \\ i_4 = i_q \cos(\theta + \frac{2}{3}\pi) \end{cases} \tag{5}$$

Reference voltages can be simplified as $u_d = 0$ and $u_q = \omega_e \Psi_f$, and the driving signals can be obtained. Taking modulation I as an example, the driving signals and three-phase currents are shown in Fig. 5. According to the switching states of each bridge, one fundamental period is divided into segment I, II and III. In segment I, the switching state of the first and forth bridge remain unchanged, and the output currents i_1 and i_4 change from negative to positive. Compared with modulation III, the fixed switching state introduces one cycle of voltage error into the first and forth bridge. Similarly, in segment II, the switching states of the second bridge remain unchanged, and the output current changes from negative to positive. One cycle of voltage error is injected into the second bridge. In segment III, the switching states of the third bridge

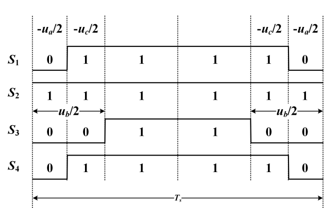

(a) Modulation I.

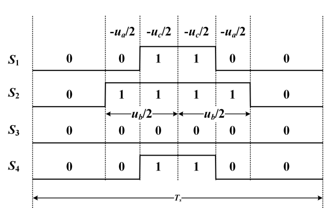

(b) Modulation II.

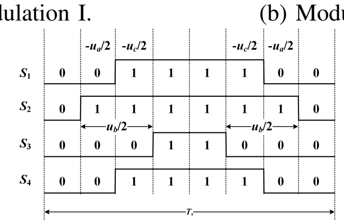

(c) Modulation III.

Fig. 3: Driving signals for four bridges.

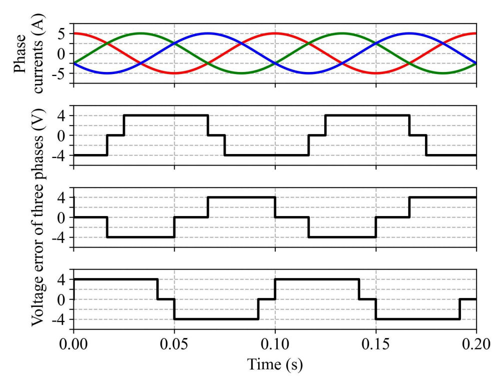

(a) Three-phase currents and voltage errors.

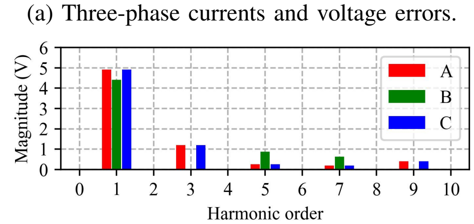

(b) Voltage error harmonics.

Fig. 4: Asymmetry of dead-time effect with modulation III.

TABLE I: Voltage harmonics injected in three phases

Segment	Fixed bridge	Affected phases
I	s_1 s_4	A C
II	s_2	A B
III	s_3	B C

remain unchanged, and the output current changes from negative to positive. One cycle of voltage error is injected into the third bridge. The phases affected by voltage harmonics during each segment are listed in Table. I. It can be seen that each phase will be injected with two cycles of harmonic voltage within one fundamental period. Compared with modulation III, modulation I and II will introduce additional even-order harmonic voltages. Three-phase currents and voltage errors are shown in Fig. 6a, and the harmonic analysis of voltage error is illustrated in Fig. 6b.

B. Extraction of Current Harmonics.

Although it is feasible to directly compensate the output voltage errors according to the bridges' current direction, accurately identifying the zero-cross points of currents is challenging. Consequently, harmonic voltage injection is adopted in this paper.

Asymmetric dead-time voltage leads to asymmetric harmonic currents in series-end winding topology. Conventional methods for suppressing current harmonics include multiple rotating reference frames and resonant regulators [14]. With multiple rotating reference frame, closed-loop control of a specific harmonic requires positive- and negative-sequence reference frames and a zero-sequence loop. However, the zero-sequence loop is one-dimensional and lacks the ability to convert AC into DC. Resonant controllers complicates parameter design and may lead to instability.

The adaline neural network (ANN) algorithm is widely applied for online parameter identification in machine control

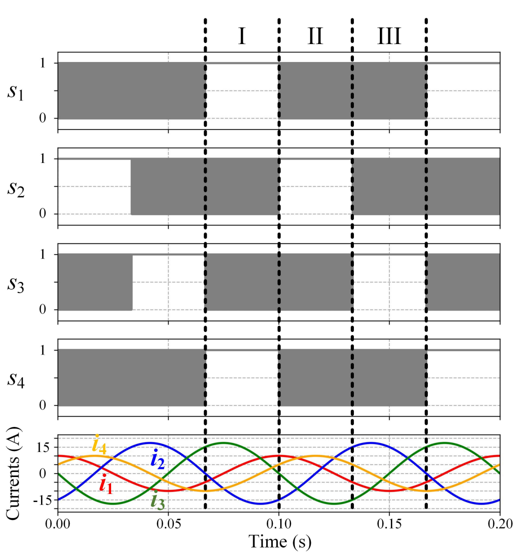

Fig. 5: Driving signals and phase currents with modulation I.

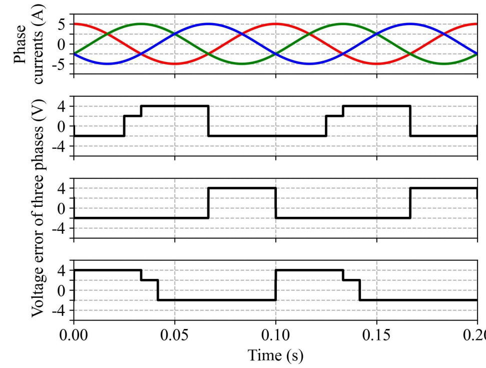

(a) Three-phase currents and voltage errors.

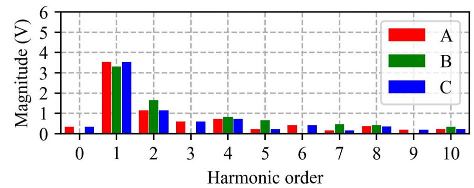

(b) Voltage error harmonics.

Fig. 6: Asymmetry of dead-time effect with modulation I.

[15]. To efficiently suppress zero-sequence harmonics without resonant regulators, a harmonic extraction method based on the ANN algorithm is adopted. The error in phase current identification can be expressed as:

$$e(n) = i_{phase}(n) - i_{obv}(n) \tag{6}$$

where $i_{phase}(n)$ represents desired output (or single-phase sampling current), $i_{obv}(n)$ represents actual output (or observed single-phase current), n represents the nth sample point.

Adaline uses the identity activation function, and the output is the weighted sum:

$$i_{obv}(n) = \mathbf{X} \cdot \mathbf{W}^T(n) \tag{7}$$

where $\mathbf{X}$ represents the harmonic components to be extracted. $\mathbf{W}(n) = \begin{bmatrix} A_0(n) & A_1(n) & B_1(n) & A_3(n) & \cdots \end{bmatrix}$ represents corresponding weight (or the amplitude of each harmonic component). To extract odd-order harmonics, $\mathbf{X}$ can be given as $\begin{bmatrix} 1 & \cos(\theta_e) & \sin(\theta_e) & \cos(3\theta_e) & \cdots \end{bmatrix}$.

Weight adjustment is based on the gradient descent method:

$$\mathrm{WA} = \frac{1}{2} \cdot e(n)^2 = \frac{1}{2} \cdot \left[i_{phase}(n) - i_{obv}(n)\right]^2 \tag{8}$$

According to chain rule and $i_{obv}(n) = \sum_{i=1}^{n} \mathbf{X}_i \mathbf{W}_i(n)$, where subscript i denotes the index of elements in the matrix, the partial derivative of WA with respect to $\mathbf{W}_i(n)$ is:

$$\frac{\partial \mathrm{WA}}{\partial \mathbf{W}_i(n)} = -\mathbf{X}_i \left[i_{phase}(n) - i_{obv}(n)\right] \tag{9}$$

The weight update rule can be expressed as:

$$\mathbf{W}_i(n+1) = \mathbf{W}_i(n) - \mu \frac{\partial \mathrm{WA}}{\partial \mathbf{W}_i(n)} = \mathbf{W}_i(n) - \mu e(n) \mathbf{X}_i \tag{10}$$

where μ is the learning rate.

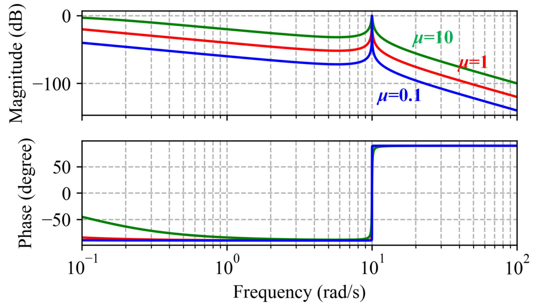

Fig. 7: Bode diagram of ANN.

Taking fundamental frequency as an example, the ANN algorithm in frequency domain can be expressed as:

$$\begin{cases} \mathbf{O}(s) = \mathbf{W_1}(s) * \frac{s}{s^2+\omega_e^2} + \mathbf{W_2}(s) * \frac{\omega_e}{s^2+\omega_e^2} \\ \mathbf{W_1}(s) = \mu\left[\mathbf{I}(s) - \mathbf{O}(s)\right] * \frac{s}{s^2+\omega_e^2} \\ \mathbf{W_2}(s) = \mu\left[\mathbf{I}(s) - \mathbf{O}(s)\right] * \frac{\omega_e}{s^2+\omega_e^2} \end{cases} \tag{11}$$

where ω_e represents the fundamental angular velocity, $*$ represents convolution, $\mathbf{I}(s)$, $\mathbf{O}(s)$, $\mathbf{W_1}(s)$ and $\mathbf{W_2}(s)$ are the Laplace transforms of $i_{obv}(n)$, $i_{phase}(n)$, $A_1(n)$ and $B_1(n)$. The transfer function from $i_{phase}(n)$ to $i_{obv}(n)$ is simplified as:

$$tf = \frac{\mu}{s^3 + \omega^2 s + \mu} \tag{12}$$

When ω_e is given as 10, the Bode diagram is shown in Fig. 7. The ANN algorithm is similar to a bandpass filter. The magnitude of the open-loop transfer function reaches 0 at the frequency ω_e. By adjusting the parameter μ, the bandwidth of the filter can be changed. However, ANN does not derive harmonic frequencies through differentiation of θ_e. It significantly enhances the precision of harmonic extraction.

C. Elimination of Dead-time Voltage Error.

With ANN algorithm, specific harmonics can be extracted from phase currents. Taking fundamental frequency as an example, three-phase currents can be expressed as:

$$\begin{cases} i_{a1} = a_1\cos(\theta_e) + b_1\sin(\theta_e) \\ i_{b1} = a_2\cos(\theta_e) + b_2\sin(\theta_e) \\ i_{c1} = a_3\cos(\theta_e) + b_3\sin(\theta_e) \end{cases} \tag{13}$$

According to (13), the sampling currents in positive-sequence reference frame can be expressed as:

$$\begin{cases} i_{dp} = \frac{1}{6}(2a_1 - a_2 - a_3 + \sqrt{3}b_2 - \sqrt{3}b_3) \\ +X_1\cos(2\theta_e) + Y_1\sin(2\theta_e) \\ i_{qp} = \frac{1}{6}(\sqrt{3}a_2 - \sqrt{3}a_3 - 2b_1 + b_2 + b3) \\ +X_2\cos(2\theta_e) + Y_2\sin(2\theta_e) \\ i_0 = \frac{1}{3}(a_1 + a_2 + a_3)\cos(\theta_e) + \frac{1}{3}(b_1 + b_2 + b_3)\sin(\theta_e) \end{cases} \tag{14}$$

In negative-sequence, the sampling currents can be expressed as:

$$\begin{cases} i_{dn} = \frac{1}{6}(2a_1 - a_2 - a_3 - \sqrt{3}b_2 + \sqrt{3}b_3) \\ +X_3\cos(2\theta_e) + Y_3\sin(2\theta_e) \\ i_{qn} = \frac{1}{6}(\sqrt{3}a_2 - \sqrt{3}a_3 + 2b_1 - b_2 - b_3) \\ +X_4\cos(2\theta_e) + Y_4\sin(2\theta_e) \\ i_0 = \frac{1}{3}(a_1 + a_2 + a_3)\cos(\theta_e) + \frac{1}{3}(b_1 + b_2 + b_3)\sin(\theta_e) \end{cases} \tag{15}$$

The subscripts p and n denote parameters in the positive- and negative-sequence reference frames.

The DC components refer to the currents to be extracted in positive- and negative-sequence, while the AC components refer to the coupling between positive- and negative-sequence. The extracted positive-, negative- and zero-sequence fundamental frequency currents can be expressed as:

$$\begin{cases} i_{dp} = \frac{1}{6}(2a_1 - a_2 - a_3 + \sqrt{3}b_2 - \sqrt{3}b_3) \\ i_{qp} = \frac{1}{6}(\sqrt{3}a_2 - \sqrt{3}a_3 - 2b_1 + b_2 + b3) \\ i_{dn} = \frac{1}{6}(2a_1 - a_2 - a_3 - \sqrt{3}b_2 + \sqrt{3}b_3) \\ i_{qn} = \frac{1}{6}(\sqrt{3}a_2 - \sqrt{3}a_3 + 2b_1 - b_2 - b_3) \\ i_0 = \frac{1}{3}(a_1 + a_2 + a_3)\cos(\theta_e) + \frac{1}{3}(b_1 + b_2 + b_3)\sin(\theta_e) \end{cases} \tag{16}$$

The extraction of other harmonics follows the same principle.

With the extracted current harmonics, positive- and negative-sequence closed-loop control can be achieved by PI controllers in rotating reference frames as shown in Fig. 9. The overall block diagram illustrating the control principle is presented in Fig. 8, where the fundamental frequency, 3rd-, 5th and 7th-order harmonics are taken into consideration.

Because the extracted zero-sequence current is one-dimensional AC and cannot be directly controlled in a rotating reference frame, a orthogonal signal can be introduced. Conventional phase shift algorithms [16], [17] lead to a quarter-

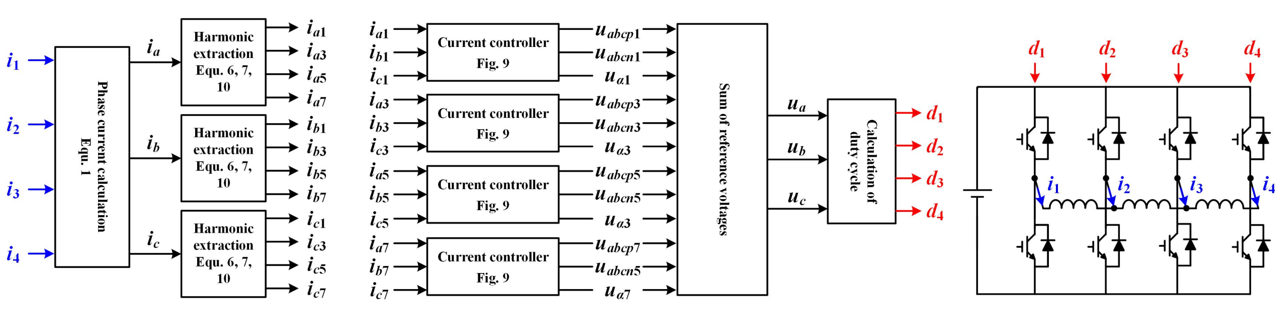

Fig. 8: Overall block diagram of the controller.

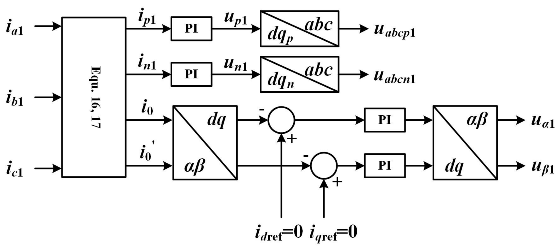

Fig. 9: Closed-loop control of d-, q- and zero-axis currents.

period delay or complicates parameter design. In this paper, the orthogonal signals is directly derived according to (16):

$$i_0' = \frac{1}{3}(a_1 + a_2 + a_3)\cos\left(\theta_e - \frac{\pi}{2}\right) + \frac{1}{3}(b_1 + b_2 + b_3)\sin\left(\theta_e - \frac{\pi}{2}\right) \quad (17)$$

With Park transformation, AC signals i_0 and $i_0{}'$ can be converted into DC signals, and closed-loop control with PI controllers can be realized.

IV. Experimental Results

Experiments have been performed based on the OEW-PMSM drive system with its picture shown in Fig. 10. The drive system includes a six-phase inverter, a prototype OEW-PMSM, and a digital control board. The digital control board is based on TMS320F28377 DSP. The sampling frequency and insulated gate bipolar translator (IGBT) switching frequency are both 10kHz. Phase currents are tested by LF 205-S/SP3 current transducers.

A. Comparison Between Modulation I, II and III.

The three-phase reference voltages are given as symmetrical sinusoidal signals, and the driving signal for the fourth bridge is the same as that for the first bridge. The driving signals of modulation III are shown in Fig. 11c. With modulation I and II, the four bridges are sequentially in a fixed switching state, and the driving signals are shown in Fig. 11a and Fig. 11b.

The harmonic analysis can be categorized into two aspects: low-frequency harmonics (considering harmonics up to 10th-order) and high-frequency harmonics (considering harmonics above 1 kHz). Low-frequency harmonics are primarily induced by dead-time voltage. High-frequency harmonics arise from switching operations.

Three-phase current harmonic analysis is shown in Fig. 12. Asymmetric voltage errors lead to significant asymmetry in three-phase currents. With modulation III, the dead-time voltage error mainly consists of odd-order harmonics and excludes even-order harmonics. It leads to fundamental frequency, 3rd-, 5th-, 7th- and 9th-order harmonics in three-phase currents as shown in Fig. 12c. With method I and II, the fixed switching states introduce even-order harmonic voltages into three phases, and corresponding even-order harmonics appear in the phase currents. The harmonic analysis of three-phase currents aligns with the dead-time voltage harmonic analysis.

The comparison between high-frequency current harmonics can be done through the harmonic distortion. Harmonic distortion can be calculated as:

$$\mathrm{HD} = \sqrt{\frac{\sum_{n=1000}^{N} V_n^2}{V_1^2}} \quad (18)$$

where V_1 is the amplitude of the fundamental frequency,

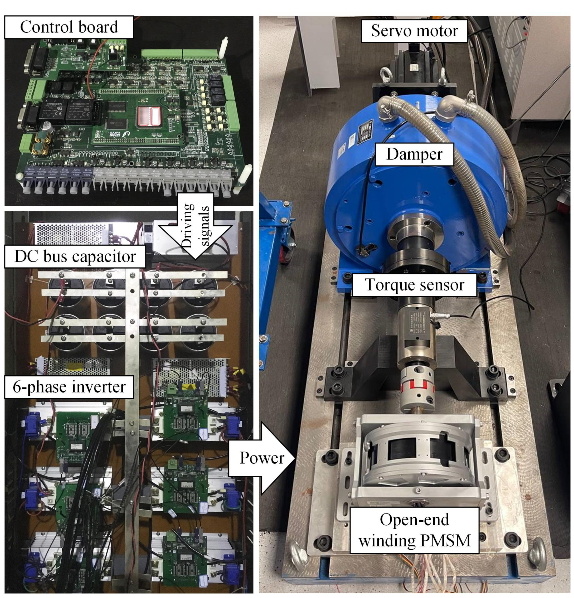

Fig. 10: Picture of the OEW-PMSM drive system.

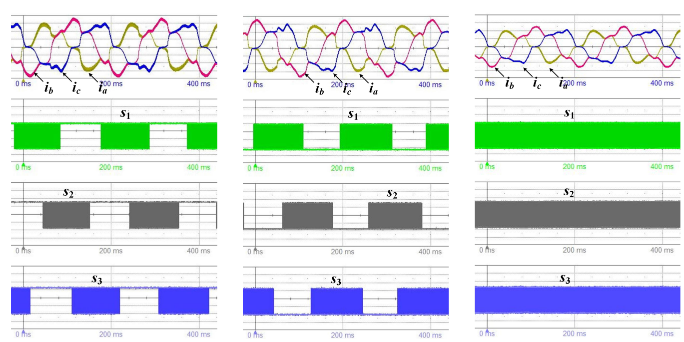

(a) Modulation I. (b) Modulation II. (c) Modulation III.

Fig. 11: Three-phase currents and driving signals.

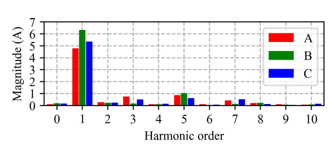

(a) Modulation I.

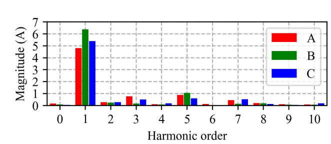

(b) Modulation II.

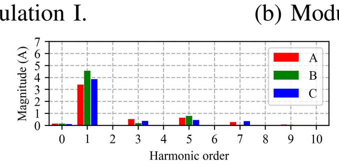

(c) Modulation III.

Fig. 12: Three-phase currents harmonic analysis.

TABLE II: Harmonic Distortion of Currents Above 1 kHz

Modulation	Phase A	Phase B	Phase C
I	5.45%	2.89%	3.28%
II	5.14%	2.74%	3.04%
III	4.20%	2.33%	2.61%

V_n is the amplitude of the nth-order harmonic. N is the highest harmonic number considered. The switching frequency is set as 10 kHz, and harmonic currents above 1 kHz are considered. The high-frequency harmonic distortion caused by modulation is shown in Table. II. Because modulation III evenly distributes the zero voltage vector to both ends and the middle of one control cycle, the phase current harmonic distortion is lower than modulation I and II.

Because modulation I and II have similar performance, only waveforms of modulation I and III will be presented in the subsequent experimental results.

B. Dead-time Compensation.

When fundamental frequency, 3rd-, 5th-, 7th-order current harmonics are closed-loop controlled and zero-sequence loop is not adopted, the fundamental frequency and 3rd-order harmonic current extracted through ANN algorithm are shown in Fig. 13. The i_q reference is 4A, and other references are all given as 0. At 0.8 seconds, the dead-time compensation algorithm is applied. Before compensation, the sampling fundamental frequency currents of each component deviate from the ideal values, i.e., $a\_\cos(\theta) = 0$, $a\_\sin(\theta) = -4$, $b\_\cos(\theta) = 2\sqrt{3}$, $b\_\sin(\theta) = 2$, $c\_\cos(\theta) = -2\sqrt{3}$, $c\_\sin(\theta) = 2$. After compensation, the sampling currents converge to the ideal values and all 3rd-order harmonics converge to 0. It means that extracting harmonic currents by ANN algorithm and conducting closed-loop control in the rotating reference frames is an effective method for suppressing rotating harmonics.

Under steady-state conditions, three-phase currents and harmonic analysis are shown in Fig. 14. Three-phase currents show significant asymmetry. Although current harmonics are suppressed in the rotating reference frames, these harmonics still exist in phase currents.

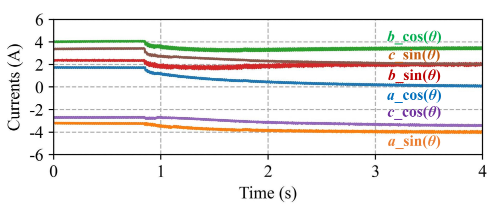

(a) Fundamental frequency.

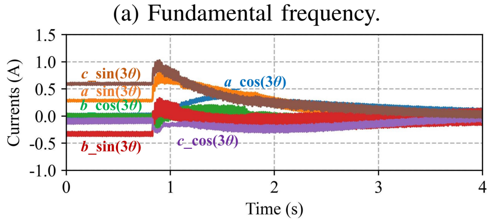

(b) 3rd-order harmonics.

Fig. 13: Currents extracted through ANN algorithm.

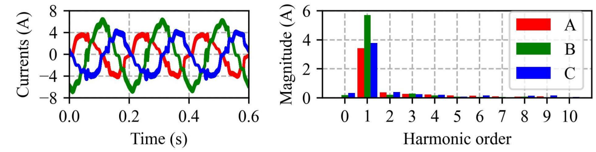

(a) Modulation I.

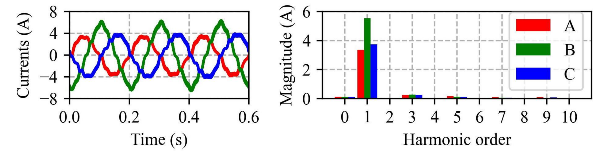

(b) Modulation III.

Fig. 14: Three-phase currents and harmonic analysis without zero-sequence loop.

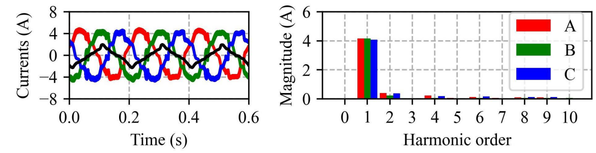

(a) Modulation I.

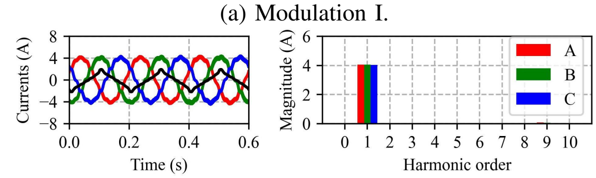

(b) Modulation III.

Fig. 15: Three-phase currents and harmonic analysis with zero-sequence removed.

According to Fig. 14, the three-phase currents without zero-sequence components and the harmonic analysis are shown in Fig. 15. The zero-sequence current is extracted and shown as the black line. For modulation I, closed-loop control are only applied in odd-order spaces. Even-order harmonics are not suppressed as shown in Fig. 15a, while the 1st-, 3rd-, 5th- and 7th-order harmonic currents are effectively suppressed. As shown in Fig. 15b, with modulation III, when the zero-sequence harmonics are ignored, three-phase currents contain no harmonic components. It indicates that the three-phase asymmetry and harmonics shown in Fig. 14 are exclusively caused by zero-sequence currents. Zero-sequence closed-loop control is essential.

When closed-loop control of zero-sequence is adopted, the extracted 5th-order zero-sequence currents are taken as an example and are shown in Fig. 16. The green line represents the current extracted by the ANN algorithm. The orange line is the waveform obtained by (17), shifting the green line by a quarter-period. After dead-time compensation, the amplitude of the sampling current and the phase-shifted waveform are synchronously decreased from above 0.2A to within 0.05A. With coordinate transformation, zero-sequence harmonics can be transformed into DC signals in dq-axes, and PI controllers can be applied for harmonic suppression.

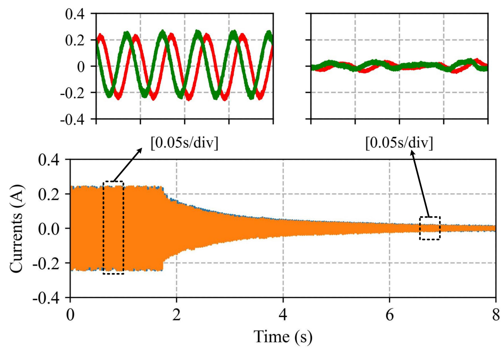

Fig. 16: Closed-loop control of 5th-order zero-sequence currents.

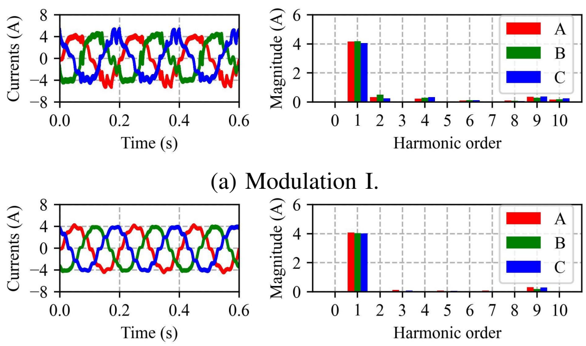

(a) Modulation I.

(b) Modulation III.

Fig. 17: Three-phase currents and harmonic analysis with zero-sequence loop.

Under steady-state conditions, three-phase currents are shown in Fig. 17. Because modulation III generates fewer dead-time voltage harmonics, closed-loop control at the 1st-, 3rd-, 5th- and 7th-order frequencies can effectively eliminate phase current harmonics. For modulation I, although the harmonics at the four frequencies are eliminated, the presence of even-order and high-order harmonics leads to significant distortion. To achieve the same control performance as modulation III, modulation I requires more harmonic loops and consumes more processor resources.

V. Conclusion

This paper proposes a modulation method for series-end winding OEW-PMSM, and the duty cycle calculation can be simplified. The asymmetric current harmonics caused by asymmetric dead-time voltage errors is analyzed, and a compensation method is proposed to eliminate dead-time effect. The closed-loop control of the zero-sequence harmonics utilizes phase shifting based on the ANN algorithm, and the closed-loop control of one-dimensional harmonics is realized in two-dimensional rotating reference frames.

In the proposed modulation algorithms, modulation I and II reduce switching losses but lead to additional harmonics in the dead-time voltages. The dead-time compensation algorithm requires more loops for both odd- and even-order harmonics. Modulation III leads to higher switching losses but the dead-time voltage errors only consist of odd-order harmonics, simplifying the dead-time compensation algorithm.

References

[1] X. Yuan, C. Zhang, and S. Zhang, "Torque ripple suppression for open-end winding permanent-magnet synchronous machine drives with predictive current control," *IEEE Transactions on Industrial Electronics*, vol. 67, DOI 10.1109/TIE.2019.2907506, no. 3, pp. 1771–1781, Mar. 2020.

[2] X. Sun, Z. Liu, A. Li, Z. Wang, D. Jiang, and R. Qu, "Self-adaptive fault-tolerant control of three-phase series-end winding motor drive," *IEEE Transactions on Power Electronics*, vol. 37, DOI 10.1109/TPEL.2022.3160747, no. 9, pp. 10 939–10 950, Sep. 2022.

[3] Z. Song, F. Zhou, Y. Yu, R. Zhang, and S. Hu, "Open-phase fault-tolerant predictive control strategy for open-end-winding permanent magnet synchronous machines without postfault controller reconfiguration," *IEEE Transactions on Industrial Electronics*, vol. 68, DOI 10.1109/TIE.2020.2984975, no. 5, pp. 3770–3781, May. 2021.

[4] H. Nian and W. Hu, "A sensorless drive strategy for open-end winding pmsm with common dc voltage based on lower switching frequency," *IEEE Transactions on Energy Conversion*, vol. 34, DOI 10.1109/TEC.2019.2896222, no. 3, pp. 1553–1562, Sep. 2019.

[5] Z. Dong, Z. Song, W. Wang, and C. Liu, "Improved zero-sequence current hysteresis control-based space vector modulation for open-end winding pmsm drives with common dc bus," *IEEE Transactions on Industrial Electronics*, vol. 70, DOI 10.1109/TIE.2022.3217600, no. 10, pp. 10 755–10 760, Oct. 2023.

[6] Y. Zhou, S. Zhang, X. Cui, C. Zhang, and X. Li, "An accurate torque output method for open-end winding permanent magnet synchronous motors drives," *IEEE Transactions on Energy Conversion*, vol. 36, DOI 10.1109/TEC.2021.3083958, no. 4, pp. 3470–3480, Dec. 2021.

[7] A. Li, D. Jiang, Z. Liu, and X. Sun, "Generalized pwm method for series-end winding motor drive," *IEEE Transactions on Power Electronics*, vol. 36, DOI 10.1109/TPEL.2020.3024591, no. 4, pp. 4452–4462, Apr. 2021.

[8] Z. Dong, Y. Chen, K. Feng, and C. Liu, "Multivector-based model predictive current control with zero-sequence current suppression for three-phase series-end winding permanent magnet synchronous motor drives," *IEEE Transactions on Transportation Electrification*, vol. 9, DOI 10.1109/TTE.2022.3220591, no. 2, pp. 3282–3294, Jun. 2023.

[9] Z. Dong and C. Liu, "Three-dimension space vector modulation for three-phase series-end winding voltage-source inverters," *IEEE Transactions on Industrial Electronics*, vol. 71, DOI 10.1109/TIE.2023.3241399, no. 1, pp. 82–92, Jan. 2024.

[10] M. S. R. Saeed, W. Song, B. Yu, Z. Xie, and X. Feng, "Low-complexity deadbeat model predictive current control for open-winding pmsm drive with zero-sequence current suppression," *IEEE Transactions on Transportation Electrification*, vol. 7, DOI 10.1109/TTE.2021.3071471, no. 4, pp. 2671–2682, Dec. 2021.

[11] Z. Dong, H. Wen, Z. Song, and C. Liu, "3-d svm for three-phase open-end winding drives with common dc bus," *IEEE Transactions on Power Electronics*, vol. 38, DOI 10.1109/TPEL.2023.3274417, no. 8, pp. 9340–9346, Aug. 2023.

[12] Z. Dong and C. Liu, "Three-dimension space vector modulation for three-phase series-end winding voltage-source inverters," *IEEE Transactions on Industrial Electronics*, vol. 71, DOI 10.1109/TIE.2023.3241399, no. 1, pp. 82–92, Jan. 2024.

[13] D. M. Park and K. H. Kim, "Parameter-independent online compensation scheme for dead time and inverter nonlinearity in ipmsm drive through waveform analysis," *IEEE Transactions on Industrial Electronics*, vol. 61, DOI 10.1109/TIE.2013.2251737, no. 2, pp. 701–707, Feb. 2014.

[14] W. Kong, Z. Yu, D. Li, R. Qu, C. Gan, S. Jia, and D. Jiang, "Comparative study of harmonic current suppression control strategies for six-phase dc-biased vernier reluctance machines," *IEEE Transactions on Industry Applications*, vol. 54, DOI 10.1109/TIA.2018.2852943, no. 6, pp. 5843–5855, Nov. 2018.

[15] Z. Liu, X. Fan, W. Kong, L. Cao, and R. Qu, "Improved small-signal injection-based online multiparameter identification method for ipm machines considering cross-coupling magnetic saturation," *IEEE Transactions on Power Electronics*, vol. 37, DOI 10.1109/TPEL.2022.3192692, no. 12, pp. 9340–9346, Dec. 2022.

[16] L. Yan, Z. Zhu, B. Shao, J. Qi, Y. Ren, C. Gan, S. Brockway, and C. Hilton, "Arbitrary current harmonic decomposition and regulation for permanent magnet synchronous machines," *IEEE Transactions on Industrial Electronics*, vol. 70, DOI 10.1109/TIE.2022.3183351, no. 5, pp. 4392–4404, May. 2023.

[17] Z. Chen, W. Kong, R. Qu, D. Li, and C. Shi, "Symmetrical components observer for lpmm back emf based on negative-sequence current injection," *IEEE Transactions on Industrial Electronics*, vol. 69, DOI 10.1109/TIE.2021.3060660, no. 2, pp. 1346–1355, Feb. 2022.

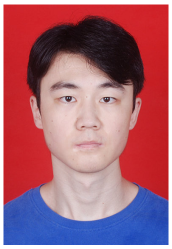

Zhi Chen received the B.E.E degree and Ph.D. degree in electrical engineering from Huazhong University of Science and Technology, Wuhan, China, in 2018 and 2023, respectively. He is currently a Postdoctoral Research Fellow with the School of Electrical and Electronic Engineering, Nanyang Technological University, Singapore. His current research focuses on control strategy of linear PM machines.

You Zhou (M'21) received the B.E.E. degree from the Chongqing University, Chongqing, China, in 2016 and the Ph. D degree from the Huazhong University of Science and Technology, Wuhan, China, in 2021, both in electrical engineering. He is currently a Postdoctoral Research Fellow with the school of electrical and electronic engineering, Nanyang Technological University, Singapore. His research interests include the design and analysis of the linear and axial-flux permanent-magnet machines.

Feifan Guo was born in Hunan, China, in 2001. He received his B.Eng. degree in Electrical Engineering and Its Automation from Wuhan University, Wuhan, China, in 2022, and his M.Sc. degree in Power Engineering from Nanyang Technological University, Singapore, in 2023. He is currently pursuing his Ph.D. degree at the School of Electrical and Electronic Engineering, Nanyang Technological University, Singapore. His current research focuses on motor control strategies.

Christopher H. T. Lee (M'12-SM'18) received his B.Eng. (First Class Honours) degree, and Ph.D. degree both in electrical engineering from Department of Electrical and Electronic Engineering, The University of Hong Kong, Hong Kong, in 2009 and 2016, respectively. He currently serves as an Associate Professor at Nanyang Technological University, Singapore, a Visiting Assistant Professor at Massachusetts Institute of Technology, United States, and also an Honorary Assistant Professor at The University of Hong Kong, Hong Kong. His research interests include Electric Machines and Drives, Renewable Energies, and Electromechanical Propulsion Technologies.